Journal of Nuclear Materials 384 (2009) 274–285

Contents lists available at ScienceDirect

Journal of Nuclear Materials

journal homepage: www.elsevier.com/locate/jnucmat

Crack propagation rate modelling for 316SS exposed to PWR-relevant conditions

M. Vankeerberghen [a,*], G. Weyns [b], S. Gavrilov [a], B. Martens [c], J. Deconinck [b]

[a] SCK•CEN, Boeretang 200, B-2400 Mol, Belgium
[b] VUB, Pleinlaan 2, B-1050 Brussels, Belgium
[c] RUG, Jozef Plateaustraat 22, 9000 Gent, Belgium

ARTICLE INFO

Article history:
Received 20 August 2008
Accepted 28 November 2008

ABSTRACT

The crack propagation rate of Type 316 stainless steel in boric acid–lithium hydroxide solutions under PWR-relevant conditions was modelled. A film rupture/dissolution/repassivation mechanism is assumed and extended to cold worked materials by including a stress-dependent bare metal dissolution current density. The chemical and electrochemical conditions within the crack are calculated by finite element calculations, an analytical expression is used for the crack-tip strain rate and the crack-tip stress is assumed equal to 2.5 times the yield stress (plane-strain). First the model was calibrated against a literature published data set. Afterwards, the influence of various variables – dissolved hydrogen, boric acid and lithium hydroxide content, stress intensity, crack length, temperature, flow rate – was studied. Finally, other published crack growth rate tests were modelled and the calculated crack growth rates were found to be in reasonable agreement with the reported ones.

1. Introduction

Type 316 stainless steel (SS316) is susceptible to stress corrosion cracking (SCC) in the coolant of pressurized-water nuclear reactors (PWRs) under some operational conditions [1]. SCC propagation involves many physico-chemical processes in the material, the environment and their mutual interface (the oxide). In the boiling water reactor (BWR) community one has come to regard a film rupture/repassivation mechanism as relevant for crack propagation [2]. This mechanism is however still under debate in respect of SCC in PWRs. Here, given that there are no readily available other mathematical models, the calculation of the CPR of 316 stainless steel in boric acid–lithium hydroxide solutions is based on a film rupture/repassivation mechanism, the finite element calculation of the chemical/electrochemical conditions within the crack and an analytical expression for the crack-tip strain rate. The SCC model is implemented in a code called CGR316BLi.

2. The SCC mechanism

The film rupture/repassivation mechanism [3] states that when the oxide film at the crack-tip is ruptured under an increasing crack-tip strain, anodic dissolution proceeds at the crack-tip until repassivation occurs. The rupture and repassivation processes recur periodically (Fig. 1). The period-averaged current density at the crack-tip can be calculated to yield [4]

$$i_{\text{avg}} = \hat{i}_0 \exp\left(\frac{\alpha F}{RT} E_{\text{tip}}\right) \frac{1}{1-m} \left(\frac{t_0}{\varepsilon_f}\right)^m \dot{\varepsilon}^m. \tag{1}$$

Using Faraday's law,

$$\dot{a} = \frac{M i_{\text{avg}}}{\rho z F}, \tag{2}$$

the CPR can be linked to this average current density at the crack-tip to yield

$$\dot{a} = \frac{M}{\rho z F} \hat{i}_0 \exp\left(\frac{\alpha F}{RT} E_{tip}\right) \frac{1}{(1-m)} \left(\frac{t_0}{\varepsilon_f}\right)^m \dot{\varepsilon}^m. \tag{3}$$

Here $\dot{a}$ is the CPR in m/s, M the atomic weight (0.055847 kg/mol), ρ the material density (7860 kg/m^3), z the charge (2 mole/mol), F Faraday's constant (96 500 C/mole), $\hat{i}_0$ a pre-exponential constant in A/m^2, α the electrode transfer coefficient (0.5), R the universal gas constant (8.31441 J/mol/K), T the temperature in K, E_{tip} the electrode potential at the tip of the crack in V, m the current decay constant for repassivation, t_o the time of exposure of the bare surface prior to re-filming (0.1 s), ε_f the strain to film rupture failure (0.0001) and $\dot{\varepsilon}$ the crack-tip strain rate in /s. Formula (3) requires the calculation of the crack-tip electrode potential E_{tip} and the crack-tip strain rate $\dot{\varepsilon}$. How CGR316BLi-calculates those is described in subsequent paragraphs.

3. The crack-tip strain rate

In the CGR316BLi model the crack-tip strain rate is calculated analytically. Various formulae can be found for the crack-tip strain

* Corresponding author. Tel.: +32 14 33 31 82; fax: +32 14 32 12 16.
E-mail address: marc.vankeerberghen@sckcen.be (M. Vankeerberghen).

0022-3115/$ - see front matter © 2009 Elsevier B.V. All rights reserved.
doi:10.1016/j.jnucmat.2008.11.034

Nomenclature

Physical constant

F	Faraday's constant (96 500) (C/mole)
R	universal gas constant (8.31441) (J/mol/K)

Calculated variables

$\dot{a}$	crack propagation rate (m/s)
p	hydrostatic pressure (Pa)
v	water velocity (m/s)
C	concentration (mol/m^3)
E_{tip}	electrode potential at the tip of the crack (V)
$\dot{\varepsilon}$	crack-tip strain rate (/s)
δ_{tip}, δ_{mouth}	crack-tip, crack-mouth opening displacement (μm)

Input parameters

T	temperature (K)
K	stress intensity (MPa$\sqrt{}$m)
L	crack length (m)
m	current decay constant for repassivation (-)
i_0	sensitization factor (-)
σ_y	yield strength (MPa)
n	work hardening exponent (Ramberg-Osgood formulation) (-)
E	Young's modulus (MPa)
v	Poisson's coefficient (-)

Calibration variable

$\dot{i}_0$	pre-exponential constant (calibration variable) (A/m^2)

Model parameters/properties

M	atomic weight (0.055847) (kg/mol)
ρ	material density (7860) or water density (kg/m^3)
μ	dynamic viscosity (kg/m/s)
z	charge (2 in (3)) (mole/mol)
α	electrode transfer coefficient (0.5) (-)
t_0	time of exposure of the bare surface prior to re-filming (0.1) (s)
ε_f	strain to film rupture failure (0.0001) (-)
β	related to the crack-tip strain rate evaluation (5.08) (-)
λ	related to the crack-tip strain rate evaluation (0.3) (-)
λ	equivalent conductivity (Scm^2)
r	location for the crack-tip strain rate evaluation (0.19×10^{-3}) (m)
D	diffusion coefficient (m^2/s)
k	reaction rate (varying)

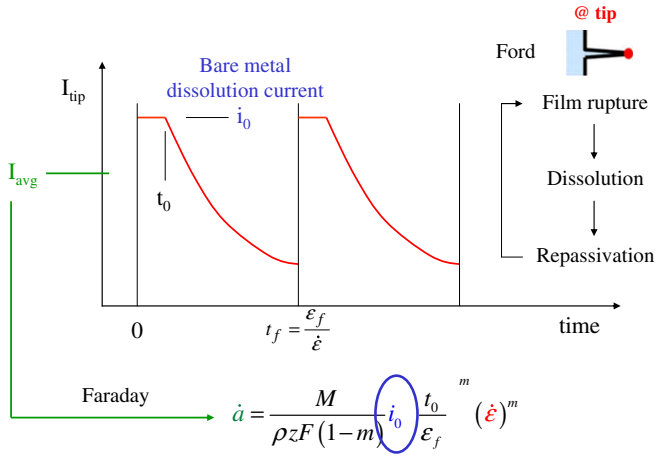

Fig. 1. The film rupture/dissolution/repassivation model [3].

rate for a growing crack in an elastic–plastic strain-hardening material. In CGR316BLi three have been implemented and the one from Hall will be used for calculations in this paper in view of perceived errors in the Shoji equations [6]

– plane-stress conditions and constant stress intensity [5]

$$\dot{\varepsilon}^{\text{Shoji}}_{\text{plane}-\sigma} = \beta \frac{\sigma_y}{E} \frac{n}{n-1} \frac{\dot{a}}{r} \left(1 + \ln\frac{R_p}{r}\right) \left(\ln\frac{R_p}{r} + \frac{1}{2}(\ln\frac{R_p}{r})^2\right)^{\frac{1}{n-1}} \quad (4)$$

– plane-strain conditions and constant stress intensity [5]

$$\dot{\varepsilon}^{\text{Shoji}}_{\text{plane}-\varepsilon} = \beta \frac{\sigma_y}{E} \frac{n}{n-1} \frac{\dot{a}}{r} (\ln\frac{R_p}{r})^{\frac{1}{n-1}} \quad (5)$$

– plane-strain conditions and constant stress intensity [6]

$$\dot{\varepsilon}^{\text{Hall}}_{\text{plane}-\varepsilon} = 2\beta' \frac{\sigma_y}{E} \frac{n}{n-1} \frac{\dot{a}}{r} (\ln\frac{R_p}{r})^{\frac{n+1}{n-1}} \quad (6)$$

R_p is the size of the plastic zone,

$$R_p = \lambda \left(\frac{K}{\sigma_y}\right)^2. \quad (7)$$

In these formulae $\dot{\varepsilon}$ is the crack-tip strain rate in /s, $\dot{a}$ the CPR in m/s, K the stress intensity in MPa$\sqrt{}$m, σ_y the yield strength in MPa, E Young's modulus in MPa, n the work-hardening exponent in the Ramberg–Osgood strain hardening law, β and λ are constant (5.08 and 0.3, respectively) and r is the location for the crack-tip strain rate evaluation (0.19 mm).

4. Crack-tip electrode potential

In the CGR316BLi model the crack-tip electrode potential is calculated based on computational electrochemistry. Through finite element modelling one obtains the chemical and electrochemical conditions in the crack's internal and external environment. The details of the modelling are described in the points below.

4.1. Crack geometry

A tapered crack geometry as shown in Fig. 2 has been assumed. The crack-tip δ_{tip} and crack mouth δ_{mouth} opening can, respectively, be expressed as [7]

$$\varepsilon_{tip}[\text{m}] = 0.6(1-\nu^2)\frac{K[\text{MPa}\sqrt{\text{m}}]^2}{E[\text{MPa}]\sigma_y[\text{MPa}]} \quad (8)$$

and (based on data in [7])

$$\delta_{mouth}[\mu\text{m}] = \delta_{tip}[\mu\text{m}] + 6.803 \times 10^{-4} \cdot K[\text{MPa}\sqrt{\text{m}}] \cdot L[\text{mm}] \cdot E[\text{GPa}]. \quad (9)$$

K is the stress intensity in MPa$\sqrt{}$m, ν Poisson's ratio, E Young's modulus in MPa, σ_y the yield strength and L the crack length in mm.

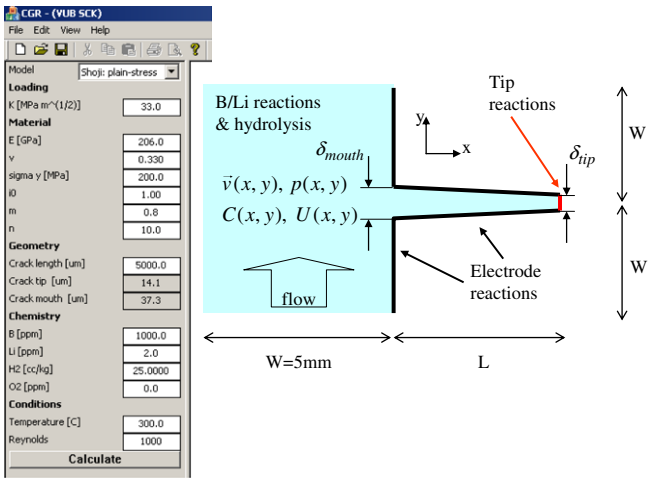

Fig. 2. The CGR316BLi input interface (left) and a schematic of the model (right).

4.2. The chemical system

The following six homogeneous reactions are considered for the aqueous boric acid–lithium hydroxide solution

$$B(OH)_3 + OH^- \Longleftrightarrow B(OH)_4^- \tag{10}$$

$$B(OH)_4^- + B(OH)_3 \Longleftrightarrow B_2(OH)_7^- \tag{11}$$

$$B_2(OH)_7^- + B(OH)_3 \Longleftrightarrow B_3(OH)_{10}^- \tag{12}$$

$$Li^+ + OH^- \Longleftrightarrow Li(OH) \tag{13}$$

$$Li^+ + B(OH)_4^- \Longleftrightarrow LiB(OH)_4 \tag{14}$$

$$H_2O \Longleftrightarrow H^+ + OH^-. \tag{15}$$

The rate constants associated with these reactions are listed in Table 1. In order to consider hydrolysis of metal cations the following heterogeneous reactions are added

$$M^{2+} + H_2O \rightarrow M(OH)^+ + H^+ \tag{16}$$

$$M(OH)^+ + H_2O \rightarrow M(OH)_2 \downarrow + H^+ \tag{17}$$

with forward reaction rates of 1×10^5, corresponding to a low solubility of metal cations.

4.3. The electrode reactions

All walls, internal and external to the crack, are considered to be 316 stainless steel and three electrochemical reactions, the hydrogen reaction (HR), the oxygen reaction (OR) and the metal dissolution reaction (MD), are assumed to occur in parallel on a natural oxide layer.The hydrogen formation reaction (HR)

$$2H^+ + 2e^- \Longleftrightarrow H_2 \tag{18}$$

has the electrode kinetics

$$i_{HR} = 1.682[H_2]\exp\left(\frac{2\times 0.099F}{RT}E\right) - 7.89\times 10^{-4}[H^+] \times \exp\left(\frac{-2\times 0.45F}{RT}E\right) \tag{19}$$

where $[H_2]$ is the local concentration of dissolved hydrogen in mol/m^3, $[H^+]$ the local concentration of the proton, E the local electrode potential and F, R and T have their usual meaning.

The oxygen reaction (OR) is implemented as

$$O_2 + 4e^- + 2H_2O \rightarrow 4OH^- \tag{20}$$

with electrode kinetics

$$i_{OR} = -0.18[O_2]^{0.66}\exp\left(\frac{-4\times 0.17F}{RT}E\right) \tag{21}$$

where $[O_2]$ is the local concentration of dissolved oxygen in mol/m^3, E the local electrode potential and F, R and T have their usual meaning. The oxygen reaction is implemented in the software but is not relevant for the deaerated conditions analysed further in this paper.

The metal dissolution reaction (MD) is implemented as

$$M \rightarrow M^{2+} + 2e^- \tag{22}$$

with a constant value for the current density of $i_{MR} = 0.012$ A/m^2 at all metallic surfaces except at the crack-tip where the electrode kinetics can be derived by combining Eqs. (1)–(3) and one of the Eqs. (4)–(6), to yield

$$i_{avg} = \left[\hat{i}_0\exp\left(\frac{\alpha F}{RT}E_{tip}\right)\frac{1}{1-m}\left(\frac{t_0}{\varepsilon_f}\frac{M}{\rho zF}G\right)^m\right]^{\frac{1}{1-m}}. \tag{23}$$

The notations have been described previously and $G = \dot{\varepsilon}/\dot{a}$ is calculated from one off the Eqs. (4)–(6).

Table 1
CGR316BLi boric acid–lithium hydroxide reactions and their rates.

Boric acid–lithium hydroxide reactions	k_f and k_b (for concentrations in mol/kg)
$B(OH)_3 + OH^- \Longleftrightarrow B(OH)_4^-$	$k_f = Q_1/\rho$ where $Q_1 = 10^{pQ_1}$ $k_b = 1$
$B(OH)_4^- + B(OH)_3 \Longleftrightarrow B_2(OH)_7^-$	$k_f = P_2/\rho$ where $P_2 = Q_2/Q_1$ and $Q_2 = 10^{pQ_2}$ $k_b = 1$
$B_2(OH)_7^- + B(OH)_3 \Longleftrightarrow B_3(OH)_{10}^-$	$k_f = P_3/\rho$ where $P_3 = Q_3/Q_2$ and $Q_3 = 10^{pQ_3}$ $k_b = 1$
$Li^+ + OH^- \Longleftrightarrow Li(OH)$	$k_f = Q_6/\rho$ where $Q_6 = 10^{pQ_6}$ $k_b = 1$
$Li^+ + B(OH)_4^- \Longleftrightarrow LiB(OH)_4$	$k_f = Q_7/\rho$ where $Q_7 = 10^{pQ_7}$ $k_b = 1$
$H_2O \Longleftrightarrow H^+ + OH^-$	$k_f = k_b\ K_w\ \rho^2$ where $K_w = 10^{pKw}$ $k_b = 6.62\times 10^{10} + 1.48\times 10^9\ T_c + 1.28\times 10^7\ T_c^2 - 6.03\times 10^4\ T_c^3 + 128\ T_c^4$

$pQ_1 = 1573.21/T + 28.6059 + 0.012078\ T - 13.2258\log_{10}(T)$.
$pQ_2 = 2756.1/T - 18.966 + 5.835\log_{10}(T)$.
$pQ_3 = 3339.5/T - 8.084 + 1.497\log_{10}(T)$.
$pQ_6 = \log_{10}(1.99)$.
$pQ_7 = \log_{10}(2.12)$.
$pK_w = -4.098 - 3245.2/T + 2.2363\times 10^5/T^2 - 3.9984\times 10^7/T^3 + (13.957 - 1262.3/T + 8.5641\times 10^5/T^2)\log(\rho/1000)$.

Table 2
CGR316BLi diffusion coefficients for ionic (a), dissolved (b) and neutral (c) species in a boric acid–lithium hydroxide solution.

(a)		
Ionic species	z	$\lambda^{298\ K}$ (S cm^2/equiv)
H^+	1	350
OH^-	−1	199
$B(OH)_4^-$	−1	40
$B_2(OH)_7^-$	−1	34
$B_3(OH)_{10}^-$	−1	27
Li^+	1	39
M^{2+}	2	39
$M(OH)^+$	1	39
$D^T = \frac{1}{10}\frac{\lambda^{298K}}{z^2}\frac{\mu_{298K}}{\mu_T}\frac{T}{298}\frac{RT}{\rho F^2}$		
(b)		
Dissolved species	D^T (m^2/s)	
O_2	$8.03\times10^{-7}e^{(-14600/RT)}$	
H_2	$10^{-4}e^{(-5.700267-296.7439/T-288379.2/T^2)}$	
(c)		
Neutral species	$D^{298\ K}$ (m^2/s)	
H_2O	1	
$B(OH)_3$	2.0×10^{-9}	
$Li(OH)$	2.0×10^{-9}	
$Lib(OH)_4$	2.0×10^{-9}	
$D^T = D^{298K}\frac{\mu_{298K}}{\mu_T}\frac{T}{298}$		

4.4. The environment

Transport of ionic and dissolved species in the environment is modelled using dilute solution theory [8]. The Nernst–Planck equation describes transport due to diffusion, electro-migration and convection for every species i, i.e.

$$\vec{N}_i = -D_i\vec{\nabla}C_i - \frac{F}{RT}z_iD_iC_i\vec{\nabla}U + C_i\vec{v} \quad \forall i, \tag{24}$$

where subscript i refers to the species' number, $\vec{N}_i$ is the flux in mol/(m^{2}s), C_i is the concentration in mol/m^3, z_i the charge, D_i the diffusion coefficient in m^2/s, U the solution potential in V and $\vec{v}$ the flow velocity in m/s. R, F and T have their usual meaning. Conservation of mass requires that

$$\frac{\partial C_i}{\partial t} = -\vec{\nabla}\vec{N}_i + \sum_k R_{k,i} \quad \forall i, \tag{25}$$

where $R_{k,,i}$ is the production rate of species i in reaction k. One additional equation, the Poisson equation, is needed to solve for the solution potential, i.e.

$$\nabla^2 U = -\frac{F}{\varepsilon}\sum_{i=1}^{n} z_iC_i, \tag{26}$$

where ε is the permittivity of the solution in C^0/(Nm^2). The diffusion coefficients for the various species are listed in Table 2. The conductivity κ of the solution can be calculated on the basis of the Nernst–Einstein relation.

$$\kappa = \frac{F^2}{RT}\sum_{i=1}^{n} z_i^2D_iC_i. \tag{27}$$

The full system of $n + 1$ equations, where n is the number of species in the solution, is solved using a finite element code [9] and yields the concentrations c_i and the solution potential U in the electrochemical system. The fluid flow is modelled using the incompressible Navier–Stokes and the continuity equations

$$\rho_w\left(\frac{\partial\bar{v}}{\partial t} + (\bar{v}\cdot\bar{\nabla})\cdot\bar{v}\right) = \mu\bar{\nabla}^2\bar{v} - \bar{\nabla}p, \tag{28}$$

$$\bar{\nabla}\cdot\bar{v} = 0, \tag{29}$$

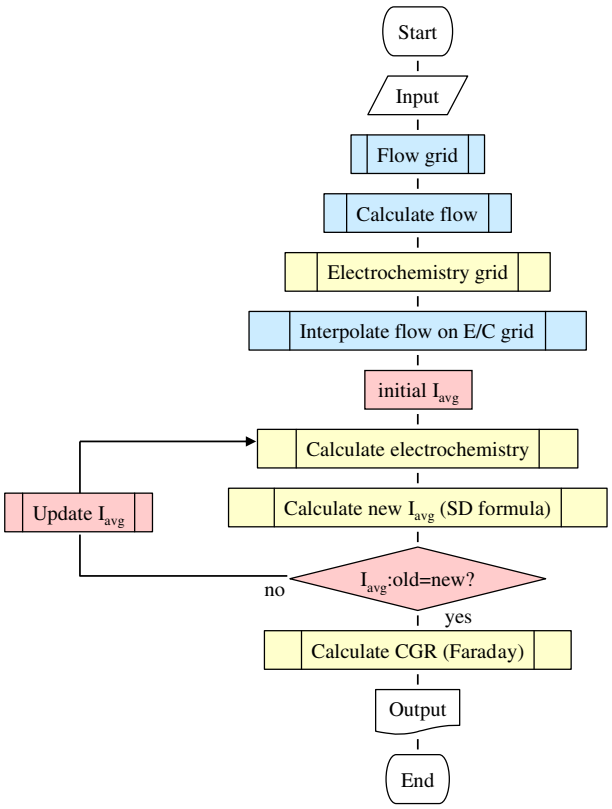

Fig. 3. Flow chart of the CGR316BLi program.

where ρ_w is the water density in kg/m^3 (calculated property), p is the hydrostatic pressure in Pa (calculated variable), v the velocity in m/s (calculated variable) and μ the dynamic viscosity in kg/m/s (calculated property). The solution of these equations yields the velocity v and pressure ρ at each point. The inlet flow conditions are given in the form of a Reynolds number defined as follows:

$$\mathrm{Re} = \frac{\rho vL}{\mu} \tag{30}$$

with ρ the density in kg/m^3 (calculated parameter), L a characteristic length in m (here taken the width of the channel 5 mm), μ the dynamic viscosity in kg/m/s and v the central velocity into the flow channel in m/s. In the simulations a Re of 1000 gives a typical velocity of about 0.04 m/s in the centre of the channel. CGR316BLi is presently limited to laminar flow.

5. Computer program

CGR316BLi (Crack Growth Rate for 316 stainless steel in Boric acid–Lithium hydroxide solutions) is a code for calculating the CPR of a stainless steel crack in a boric acid–lithium hydroxide solution under PWR-relevant conditions. The CGR316BLi input screen and a schematic of the model are shown in Fig. 2. The steps in the calculation are schematically shown in Fig. 3. First a flow grid is made and the flow is calculated (finite element-based). Then the electrochemistry grid is prepared and the flow is interpolated on it. Next, the electrochemical calculations are started (finite element-based). However, implementing (23) at the crack-tip yielded convergence problems. Hence, an initial current density is assumed at the crack-tip and slowly changed until (23) is met. Finally, the crack propagation rate is calculated using Faraday's law. CGR316BLi input parameters, their ranges and default values are given in Table 3.

Table 3
CGR316BLi input parameters, their ranges and default values.

Parameter	Unit	Abbreviation	Range	Default
Loading				
Stress intensity	MPa$\sqrt{m}$	K	[10–50]	33
Material				
Elasticity modulus	GPa	E	[150–300]	200
Poisson's ratio	–	v	[0.25–0.35]	0.33
Yield strength	MPa	σ_y	[100–1000]	200
Sensitization factor	–	i_0	[0.01–100]	1
Repassivation decay constant	–	m	[0.1–0.9]	0.8
Work hardening exponent	–	n	[2–15]	10
Geometry				
Crack length	mm	L	[1–10]	5
Environment				
Boron acid concentration	ppm	B	[0–5000]	1000
Lithium hydroxide concentration	ppm	Li	[0–10]	2
Dissolved hydrogen concentration	cc/kg	H_2	[0–50]	25
Temperature	°C	T	[25–350]	300
Reynolds numbers	–	Re	[0–2000]	1000

Table 4
Calibration data set for CGR316BLi. Compiled from graphs and tables in [10] and private communication with Arioka.

Cold work	K (MPa$\sqrt{m}$)	σ_y (MPa)	n (-)	T (°C)	CGR (m/s)
Cold work dependence					
5% CW	26	243	4.74	320	6.00E-12
	35	243	4.74	320	1.50E-11
10% CW	25.5	345	7.22	320	3.20E-11
	26.5	345	7.22	320	1.60E-11
	35	345	7.22	320	3.60E-11
15% CW	14	495	6.90	320	4.50E-12
	20	495	6.90	320	4.40E-11
	24.5	495	6.90	320	4.40E-11
	27	495	6.90	320	6.50E-11
	37	495	6.90	320	1.10E-10
20% CW	21.5	572	8.35	320	6.40E-11
	25	572	8.35	320	1.10E-10
	30	572	8.35	320	1.10E-10
	42	572	8.35	320	1.80E-10
Temperature dependence					
20% CW	30	577	8.35	270	1.50E-11
	30	575	8.35	290	2.80E-11
	30	572	8.35	320	1.20E-10

6. Reference data set and calibration

The data published in [10] are used as a calibration dataset for the CGR316BLi code. Some of the data are given in Table 4 and further inputs include:

- a Young's modulus E of 175 GPa @ 320 °C, 177 GPa @ 290 °C and 179 GPa @ 270 °C;
- a Poisson's ratio of 0.3;
- a sensitization multiplication factor of 1;
- a repassivation constant of 0.5;
- environmental conditions of 500 ppmB, 2 ppmLi and 30 ccH_2/kg;
- a Reynolds number of 1000 and
- an electrochemical crevice length of 3.125 mm.

CGR316BLi is based on a two-dimensional crack geometry. Since environmental access to the crack-tip is mainly from the side of the 1/2T CT (half size compact tension specimen) the electrochemical crack length is taken to be an average one, i.e. equal to one quarter of the specimen thickness.

Previously [14–16], the bare metal dissolution current density i_0 (Fig. 1) has been taken to be electrode potential dependent, i.e.

$$i_0 \approx \exp\left\{\frac{\alpha \mathrm{FE}_{\mathrm{tip}}}{\mathrm{RT}}\right\}. \tag{31}$$

Where α is the electrode transfer coefficient, E_{tip} the electrode potential at the tip of the crack in V and F, R and T have their usual meaning. During the course of this research it became apparent that one also needs to include the stress effect [17] on the bare metal dissolution current density i_0, i.e.

$$i_0 \approx \exp\left\{\frac{V_m \sigma_{\mathrm{tip}}}{\mathrm{RT}}\right\} \tag{32}$$

where V_m is the molar volume in m^3/mol, σ_{tip} the stress at the tip of the crack in Pa and R and T have their usual meaning. Under plain strain conditions the tensile stress σ_{tip} is equal to $2.5\sigma_y$ from linear-eleastic fracture mechanics for an isotropic material using the von Mises yield criterion and $v = 0.3$ [18] and approximately $2.5\sigma_y$ from elastic–plastic fracture mechanics using large strain finite element analysis with finite geometry changes [18,19], where σ_y is the yield stress. The bare metal dissolution current density i_0 is further thermally activated, i.e.

$$i_0 \approx \exp\{\frac{-E_a}{\mathrm{RT}}\}. \tag{33}$$

Hence, the final expression reads

$$\begin{aligned} i_0 &= \hat{i}_0 \exp\left\{\frac{-E_a + \alpha \mathrm{FE}_{\mathrm{tip}} + V_m \sigma_{\mathrm{tip}}}{\mathrm{RT}}\right\} \\ &= \hat{i}_0 \exp\left\{\frac{-E_a + \alpha \mathrm{FE}_{\mathrm{tip}} + V_m (2.5\sigma_y)}{\mathrm{RT}}\right\}. \end{aligned} \tag{34}$$

When calculating the i_0-values (calibration) that make the measured (Table 4) and predicted (3) CPRs correspond we find the exponential stress relationship (32) as shown in Fig. 4. The symbols represent the calibrated i_0-values, the solid line is a best fit (V_m is allowed to vary) and the dotted line is a fit using the theoretical molar volume as calculated from $V_m = M/\rho = 7.11 \times 10^{-6} m^3$/mol, where M is the molar mass and ρ the density of the stainless steel. The extracted value for V_m is 9.48×10^{-6} m^3/mol, which is close to the theoretical molar volume. Hence, the magnitude of V_m is relatively well returned by the experimental data (Table 5). The value of $\hat{i}_0$ is used as a calibration factor and compensates for other, less-precise parameter estimates [16], e.g. the film critical strain ε_f and t_0, one of the repassivation constants.

In the paragraphs below we show the correspondence between the measured [10] and CGR316BLi-calculated CPRs.

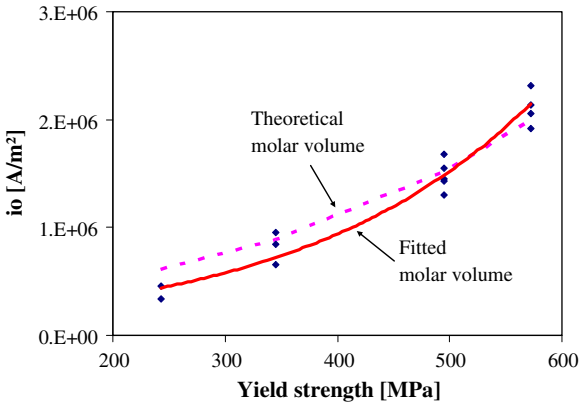

Fig. 4. Yield strength effect on the i_0-values.

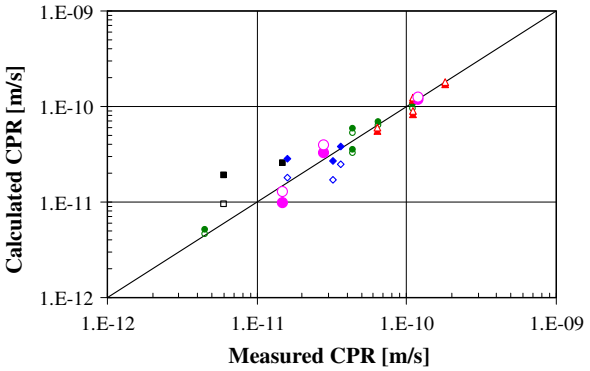

Fig. 5. Measured [10] and CGR316BLi-calculated crack propagation rates. The symbols represent various levels of cold work level: squares = 5% CW, diamonds = 10% CW, circles = 15% CW and triangles = 20% CW. The large circles correspond to various temperatures: 270 °C, 290 °C and 320 °C. Open symbols are for a fitted molar volume and closed symbols for the theoretical molar volume.

6.1. Calibration results

Fig. 5 shows the CGR316BLi-calculated CPRs against the measured [10] ones. The solid symbols correspond to a theoretical molar volume of 7.11×10^{-6} m^3/mol and the open symbols to a fitted molar volume of 9.48×10^{-6} m^3/mol. The symbols represent various levels of cold work (squares = 5% CW, diamonds = 10% CW, circles = 15% CW and triangles = 20% CW) and correspond to the first set of records in Table 4. The larger circles represent data at various temperatures (270 °C, 290 °C and 320 °C at 30 MPa$\sqrt{}$m) and corresponds to the last three records in Table 4.

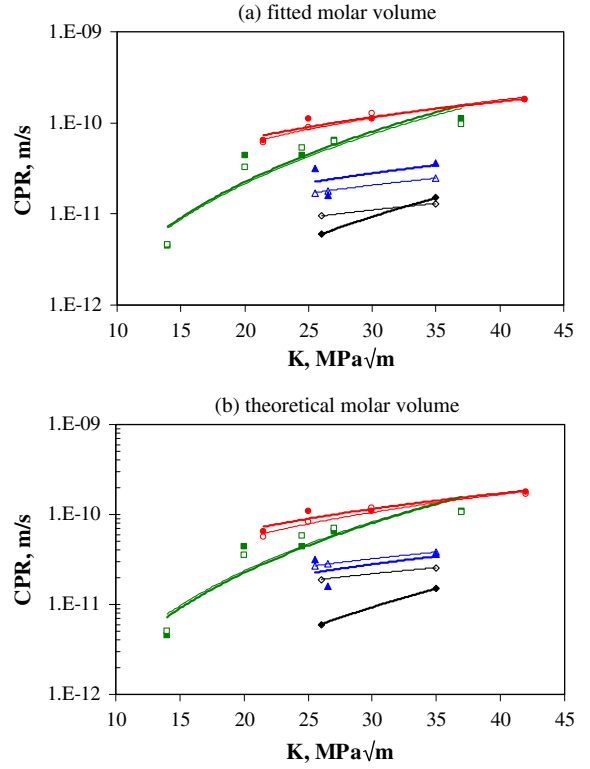

Fig. 6. The effect of stress intensity on crack propagation rate: (a) fitted molar volume, (b) theoretical molar volume. Solid symbols and thick lines correspond to the data of [10]. Open symbols and thin lines correspond to CGR316BLi-calculations. Symbols refer to the level of cold work: diamonds = 5% CW, triangles = 10% CW, squares = 15% CW and circles = 20% CW.

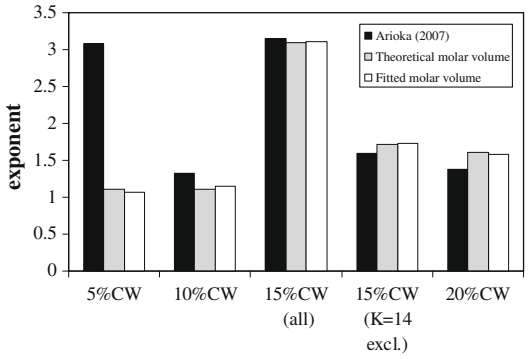

Fig. 7. The exponent b of CPR = aK^b.

6.2. Stress intensity K

Fig. 6 shows the effect of the stress intensity K on crack propagation rate. Solid symbols and thick lines correspond to the measured data [10]. The lines represent a power law fit. Open symbols and thin lines correspond to CGR316BLi-calculations. Symbols refer to the level of cold work (diamonds = 5% CW, triangles = 10% CW, squares = 15% CW and circles = 20% CW). The bottom figure corresponds to a theoretical molar volume of 7.11×10^{-6} m^3/mol and the top figure to a fitted molar volume of 9.48×10^{-6} m^3/mol. Fig. 7 shows the exponent b of CPR = aK^b, a commonly used data-fit [12]. The black, grey and open bars respectively correspond to measured data [10], CGR316BLi-calculations using a theoretical molar volume of 7.11×10^{-6} m^3/mol and CGR316BLi-calculations using a fitted molar volume of 9.48×10^{-6} m^3/mol. Two bars are shown for the 15% CW level; one including and one excluding the data point at a stress intensity of K = 14 MPa$\sqrt{}$m. Indeed, this point does not agree with the power law fit, neither experimentally, nor calculated.

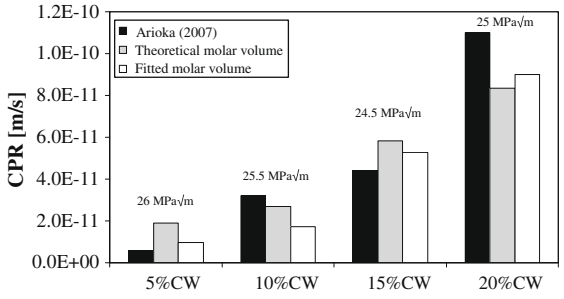

Fig. 8. The effect of the level of cold work on crack propagation rate.

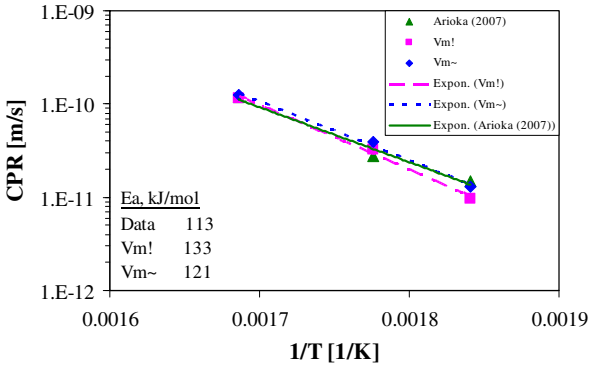

Fig. 9. The effect of temperature on crack propagation rate. V_m! theoretical molar volume. V_m~ fitted molar volume.

6.3. Cold work

Fig. 8 shows the effect of the level of cold work on CPR at approximately 25 MPa$\sqrt{m}$. The black, grey and open bars, respectively correspond to measured data [10], CGR316BLi-calculations using a theoretical molar volume of 7.11×10^{-6} m^3/mol and CGR316BLi-calculations using a fitted molar volume of 9.48×10^{-6} m^3/mol.

6.4. Temperature T

Fig. 9 shows the effect of temperature on CPR at 30 MPa$\sqrt{m}$. The thick line/triangles, thin line/squares and dotted lines/diamonds, respectively correspond to measured data [10], CGR316BLi-calculations using a theoretical molar volume of 7.11×10^{-6} m^3/mol and CGR316BLi-calculations using a fitted molar volume of 9.48×10^{-6} m^3/mol. The respective activation energies are displayed on the chart.

6.5. Profiles

Fig. 10 shows typical profiles for electrode potential, dissolved hydrogen and pH along the crack for the case '20% CW, K = 30 MPa$\sqrt{m}$, T = 320 °C and 30 ccH2/kg'.

7. Trend calculations

The trend calculations have been split into three subsets; (1) a sensitivity calculation to study the effect of less-precisely known input parameters such as the repassivation exponent m and the electrochemical crack length L, (2) a set of calculations corresponding to variations in the test condition such as the flow Re, the dissolved hydrogen concentration [H_2], the lithium concentration [Li], the operational cycle and the stress intensity K and (3) a set of calculations corresponding to variations in material characteristics such as yield strength σ_y and work hardening n. The trend calculations are single variable calculations around a selected reference case (▲ in the figures); K = 30 MPa$\sqrt{m}$, E = 175 GPa, ν = 0.3, σ_y = 572 MPa, m = 0.5, n = 8.35, L = 3125 μm, [B] = 500 ppm, [Li] = 2 ppm, [H_2] = 30 cc(STP)/kg, T = 320 °C, Re = 1000.

7.1. Sensitivity study

Fig. 11(a) shows a marked decrease of the CPR with the repassivation exponent and Fig. 11(b) a slight decrease with the crack length L.

7.2. Trend calculations, environment

Calculations show no effect of the flow rate on the CPR. Fig. 12(a) shows that the CPR decreases with the primary water hydrogen content [H_2]. Fig. 12(b) shows that the CPR decreases with the lithium concentration [Li] for two values of boric acid concentration. Fig. 12(c) shows how the CPR varies as a PWR plant goes through two operational cycles [13] (Fig. 13); cycle 1 is referred to as the constant pH-cycle and cycle 2 as the constant Li-cycle. Fig. 12(d) shows that the CPR increases with the stress intensity level.

7.3. Trend calculations, material

Fig. 14(a) shows that the CPR increases with the yield strength σ_y and Fig. 14(b) that the CPR decreases with the work hardening exponent n.

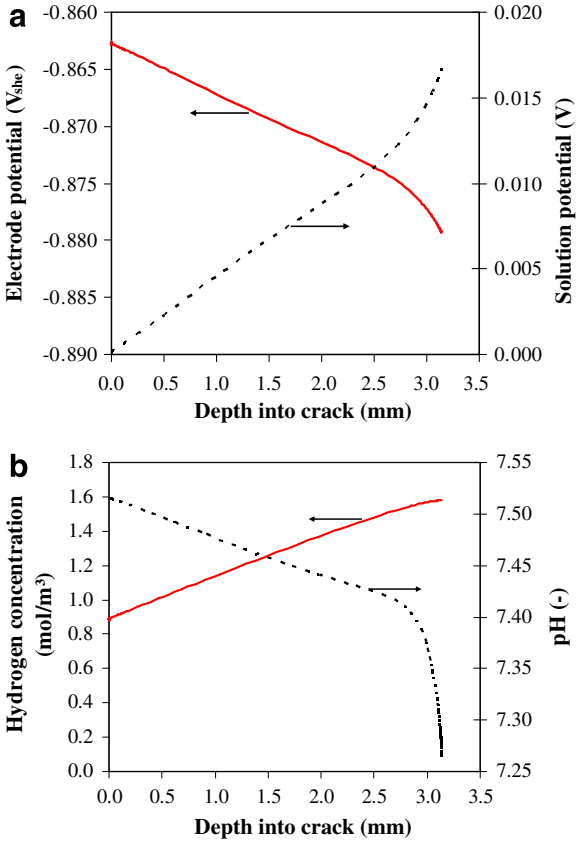

Fig. 10. Typical profiles of (a) electrode and solution potential and (b) dissolved hydrogen and pH for 20% CW 316 stainless steel, a stress intensity of 30 MPa$\sqrt{m}$, a temperature of 320 °C and a dissolved hydrogen concentration of 30 ccH_2/kg.

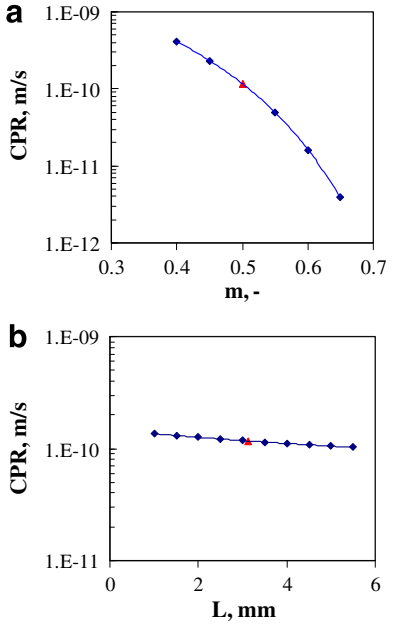

Fig. 11. Sensitivity of the crack growth rate to (a) the repassivation parameter m and (b) the electrochemical crack length L. Reference case (▲): K = 30MPa$\sqrt{m}$, E = 175 GPa, ν = 0.3, σ_y = 572 MPa, m = 0.5, n = 8.35, L = 3125 μm, [B] = 500 ppm, [Li] = 2 ppm, [H_2] = 30 cc(STP)/kg, T = 320 °C, and Re = 1000.

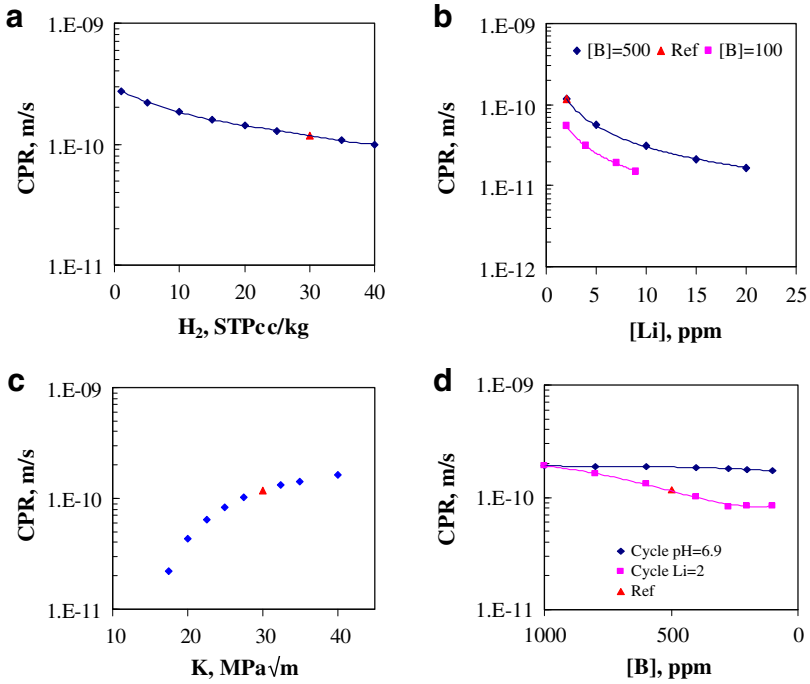

Fig. 12. Single parameter trend calculations performed with CGR316BLi: (a) dissolved hydrogen, (b) lithium concentration, (c) stress intensity and (d) water chemistry cycle. Reference case (▲): $K = 30$ MPa$\sqrt{m}$, $E = 175$ GPa, $\nu = 0.3$, $\sigma_y = 572$ MPa, $m = 0.5$, $n = 8.35$, $L = 3125$ μm, [B] = 500 ppm, [Li] = 2 ppm, [H_2] = 30 cc(STP)/kg, $T = 320$ °C and Re = 1000.

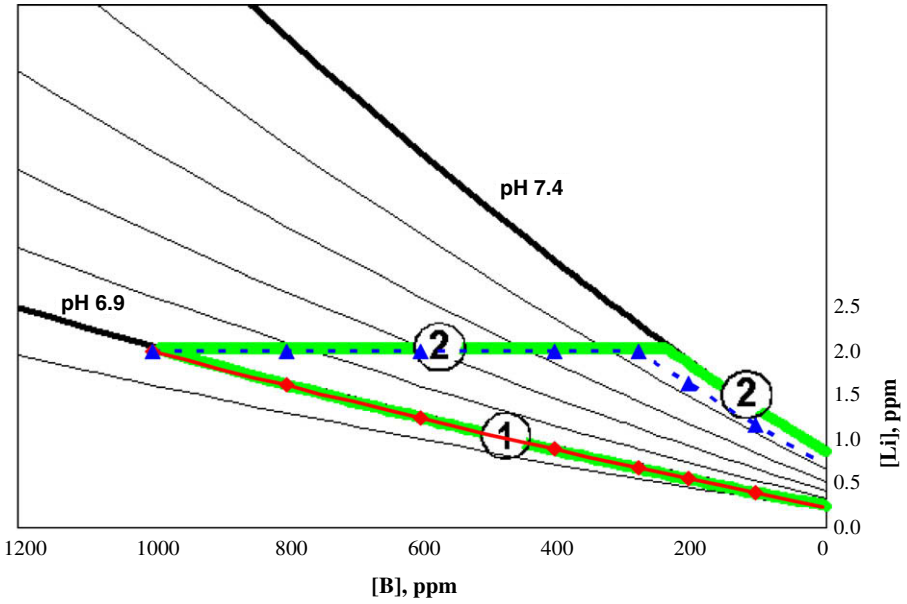

Fig. 13. Two operational boric acid–lithium hydroxide cycles. (1) A cycle with a constant pH. (2) A cycle with a constant lithium content until a pH of 7.4 is reached [13].

8. Discussion

8.1. Geometry

In CGR316BLi the crack growth rate model has been implemented for the two-dimensional geometry shown in Fig. 2. However, most crack growth rate measurements are performed on compact-tension (CT) specimens that have a three-dimensional geometry. The crack growth rate model could, in principle, be implemented for a three-dimensional CT geometry, but this would result in a dramatic increase in problem size, run time and memory requirements from the present, i.e. approximately one million degrees of freedom, 1 h of run time and two gigabyte of internal memory. In order to compare CGR316BLi-calculated and CT-measured crack growth rates the authors use the following approximate crack length. Since access to the external crack environment is principally access to the side surfaces of the CT specimen, the electrochemical crack length varies from zero to half the specimen thickness. The authors compare CGR316BLi-calculated and CT-measured crack growth rates assuming an electrochemical crack length of one quarter of the specimen thickness. The CT crack length (ASME E399) is used to determine the stress

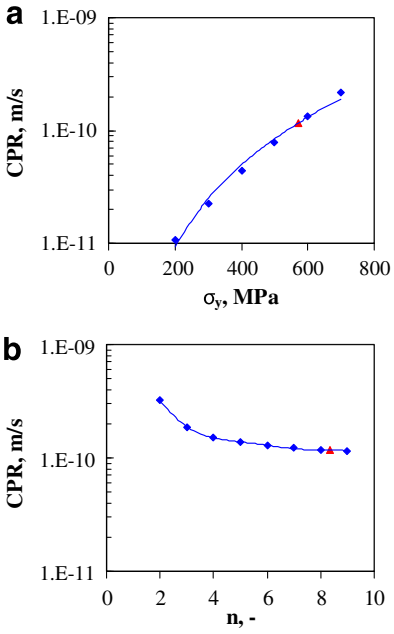

Fig. 14. Single parameter trend calculations performed with CGR316BLi: (a) yield strength, (b) work hardening exponent. Reference case (▲): $K = 30\ \mathrm{MPa}\sqrt{\mathrm{m}}$, $E = 175$ GPa, $\nu = 0.3$, $\sigma_y = 572$ MPa, $m = 0.5$, $n = 8.35$, $L = 3125$ μm, [B] = 500 ppm, [Li] = 2 ppm, [H_2] = 30 cc(STP)/kg, $T = 320$ °C and Re = 1000.

intensity K. During a CT crack growth rate test under constant load the CT (mechanical) crack length will continuously change, increasing the stress intensity K, but the electrochemical crack length will remain constant at one quarter of the specimen thickness, keeping the electrochemical conditions at the crack-tip almost constant under constant environmental conditions. If a three-dimensional geometry would be implemented a concave or convex crack front could result from a competition between mechanical (harshest in the middle) and electrochemical (harshest on the edge) loading of the crack-tip [11]. Using a two-dimensional geometry implies that one cannot model any fluid flow effects associated with wash-out of the crevice from the side of the CT specimen for that dimension is abscent.

8.2. Stress intensity

The power law fits in Fig. 6 are of the form $\mathrm{CPR} = aK^b$. The values for the exponent b are given in Fig. 7. The fit is not particularly well for a level of cold work of 15%. The reason for this is that for this level of cold work there is a data point at the relatively low K value of 14 $\mathrm{MPa}\sqrt{\mathrm{m}}$. At low K values the K dependence is greater as can also be seen from Fig. 12(c). Hence, one power law fit would not be applicable in the full K range, although it is commonly used in guidelines [12]. The CGR316BLi code reproduces properly the experimentally data, including the low K value data point.

8.3. Cold work

Previous literature published models based on the film rupture/dissolution/repassivation mechanism do not correctly model the effect of cold work. When simultaneously changing the yield strength and the work hardening exponent associated with the various levels of cold work, the CPR usually decreases with an increase in the level of cold work. Here, by including the stress effect on the bare metal dissolution current according to Gutman [17], it is shown that the CPR increases with the level of cold work as observed experimentally (Fig. 8).

To the authors' knowledge the CGR316BLi code is the only code that can presently calculate CPRs for uniformly cold worked 316 stainless in boric acid–lithium hydroxide solutions of varying composition. Furthermore, it has the potential to develop towards the calculation of component CPRs, i.e. by moving from 2D to 3D calculations. The extended film rupture/dissolution/repassivation model, including the stress effect on the bare metal dissolution current density, can however readily be implemented in other stress corrosion crack propagation models such as the FRI-model (Tohoku University's Fracture Research Institute, Professor T. Shoji [19–21]), the CEFM (Professor D.D. Macdonald, Penn State University [15–16]) or the Pledge code (GEGR, P.L. Andresen [21–23]). The FRI-model is however unable to take environment composition into account and the CEFM is restricted to a 1D calculation, making the further development of the 'CGRMatEnv'-type software a worthwhile quest.

A modified FRI-model has been developed. It includes the crack-tip strain rate equation of Hall [6] and the stress effect on the bare metal dissolution current according to Gutman [17]. The modified FRI equation for the CPR under plane-strain conditions in a CT specimen under constant load and given environmental conditions reads

$$\dot{a} = A \cdot \exp\left\{\frac{V_m \sigma_{\mathrm{tip}}}{\mathrm{RT}}\right\} \cdot \dot{\varepsilon}^m_{\mathrm{Hall}}, \tag{35}$$

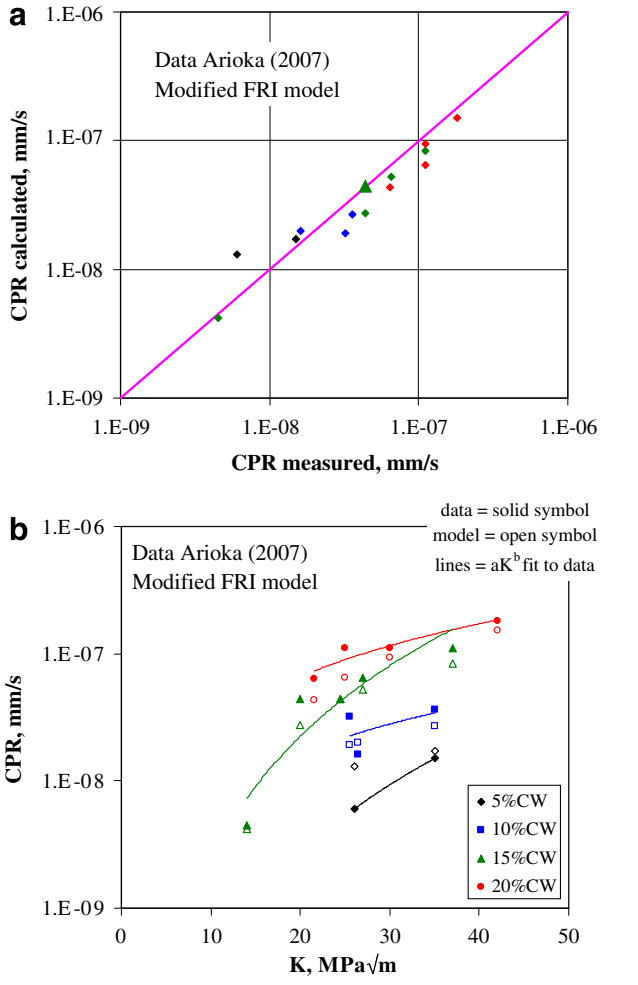

Fig. 15. Modified FRI model applied to the data presented in [10]. (a) Calculated against experimental crack growth rate. (b) The effect of stress intensity on crack propagation rate.

where $\dot{a}$ is the CPR, V_m the molar volume, σ_{tip} the stress at the crack-tip, $\dot{\varepsilon}$ the crack-tip strain rate, A a calibration constant and R and T have their usual meaning. The results are shown in Fig. 15. Good agreement between the experimentally measured and model-calculated CPRs can be observed. However, it must be noted that this modified FRI model, once calibrated in a specific environment, cannot readily yield CPR results in a different environment and that it is limited to CT specimens where the electrochemical crack length is decoupled from the mechanical crack length.

8.4. Hydrogen content

Fig. 12(a) shows that the CGR316BLi-calculated CPR decreases with the primary water hydrogen content. Fig. 18 in Ref. [24] shows a graph illustrating the effect of a switch from 1580 $ppbH_2$ ($\sim$17.7 ccH_2/kg) to 3160 $ppbH_2$ ($\sim$35.4 ccH_2/kg) for a 50% 'cool'-worked 304L stainless steel in pure water at 288 °C. Although the paper states 'no difference in growth rate' the CPR seems to slightly decrease at the higher hydrogen content. The decrease in CPR is probably due to a reduction in the electrode potential at the crack-tip.

8.5. Profiles

Fig. 10(a) shows that the potential profile in a crack in a PWR is significantly different from that in a BWR. Due to the higher conductivity and the absence of oxygen the potential drop in the crack's internal, and especially external, environment is substantially lower in a PWR than in a BWR crack. Furthermore, whereas the potential change is largest close to the mouth of the crack in a BWR crack [25], it is largest close to the tip of a crack in a PWR crack. The significant potential drop in a BWR close to the crack's mouth is related to a depletion of oxygen as one moves into the crack [25]. Under normal operating conditions this oxygen gradient is not present in a PWR crack. In a PWR crack the electrode potential changes almost linearly along the crack until one gets close to the crack-tip where the influence of the crack-tip's repassivation current becomes apparent.

Fig. 10(b) shows an increased dissolved hydrogen content and a decreased pH as one moves into the crack. The dissolved hydrogen content changes almost linearly along the crack. The pH changes pretty linearly along the crack until one gets close to the crack-tip where the influence of the crack-tip's repassivation current becomes apparent. Here the pH buffering is disturbed by metal cation injection, and subsequent hydrolysis, accompanying repassivation.

Table 5
Parameters obtained from comparing CGR316BLi-calculated and measured [10] crack growth rates.

m, -	Theoretical V_m 0.5, fitted	Fitted V_m
$\dot{i}_0$ (A/m^2)	1.4145×10^{15}	4.9772×10^{14}
E_a (kJ/mol)	110.7	108.8
V_m (m^3/mol)	(7.1052×10^{-6})	9.4908×10^{-6}

8.6. Other crack growth rate data

Ref. [26] reports CPRs on 5 mm thick CT specimens at 288 °C for unidirectional 40% cold-worked 316L stainless steel in simulated primary water with 1000 ppm boric acid, 2 ppm lithium hydroxide and an hydrogen content of 30 cc(STP)/kg water for stress intensities between 25 and 30 $MPa\sqrt{m}$. Accordingly CGR316BLi was run with the parameters listed in Table 6. First assuming that the yield strength and work-hardening exponent corresponded to the uniformly cold rolled 20% CW and then extrapolating the yield strength and work-hardening exponent to uniformly cold rolled 40% CW. The results are shown in Fig. 16.

Ref. [27] reports CPRs on 15 mm thick CT specimens for unidirectional 40% cold-worked 316L stainless steel in simulated primary water with 1000 ppm boric acid, 2 ppm lithium hydroxide and an hydrogen content between 20 and 40 cc(STP)/kg water for stress intensities between 25.4 and 65 $MPa\sqrt{m}$. Accordingly CGR316BLi was run with the parameters listed in Table 6. First assuming that the yield strength and work-hardening exponent corresponded to the uniformly cold rolled 20% CW and then extrapolating the yield strength and work-hardening exponent to uniformly cold rolled 40% CW. The results are shown in Fig. 16.

The agreement is pretty good given that we are probably not talking about the same material and type of cold working, that some input parameters (σ_y and n) are extrapolated to 40% CW, that some input variables (T, [B], K and [H_2]) are outside the calibration dataset's range and that experimental data and conditions display inter-specimen scatter.

8.7. Crack growth rate mechanism

In this paper the film rupture/dissolution/repassivation (FRDR) mechanism has been further developed in order to model the effect of cold work. In essence the bare metal dissolution current has

Table 6
Application of CGR316BLi to other literature published data.

	Ref. [26]		Ref. [27]					
K ($MPa\sqrt{m}$)	25–30	25–30	25.4–29.2	25.4–29.2	38.4–48.7	38.4–48.7	57–65	57–65
E (GPa)	177	177	177	177	177	177	175	175
ν (-)	0.3	0.3	0.3	0.3	0.3	0.3	0.3	0.3
σ_y (MPa)	575 s	723 e	575 s	723 e	575 s	723 e	575 s	723 e
i_0 (-)	1	1	1	1	1	1	1	1
m (-)	0.5	0.5	0.5	0.5	0.5	0.5	0.5	0.5
n (-)	8.35 s	9.81 e	8.35 s	9.81 e	8.35 s	9.81 e	8.35 s	9.81 e
L (μm)	1250	1250	3750	3750	3750	3750	3750	3750
[B] (ppm)	1000	1000	1000	1000	1000	1000	1000	1000
[Li] (ppm)	2	2	2	2	2	2	2	2
[H_2] (cc/kg)	30	30	30–40	30-40	30–40	30–40	20–35	20–35
T (°C)	288	288	289	289	289	289	325	325
Re (-)	1000	1000	1000	1000	1000	1000	1000	1000
Measured								
CPR (m/s)	1.6–4.2 … 9.1–13.0 × 10^{-11}		2.0–8.3 × 10^{-11}		1.0–2.4 × 10^{-10}		1.3–4.7 × 10^{-10}	
CGR316BLi-calculated								
CPR (m/s)	4.1–5.8 × 10^{-11}	7.7–12.9 × 10^{-11}	3.1–4.9 × 10^{-11}	5.9–10.6 × 10^{-11}	0.6–0.9 × 10^{-10}	1.5–2.3 × 10^{-10}	4.6–21.1 × 10^{-10}	7.9–12.9 × 10^{-10}

s = Saturated σ_y and n values.
e = Extrapolated σ_y and n values.

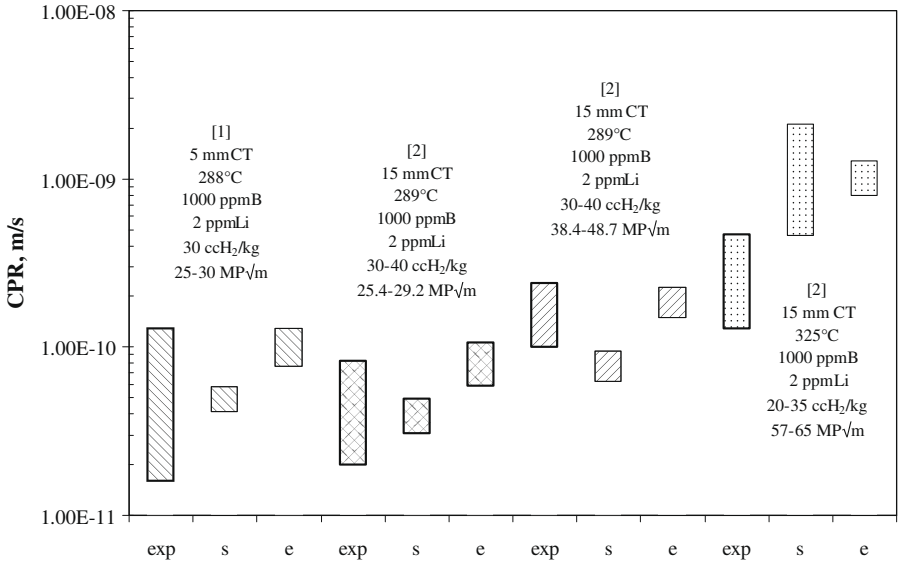

Fig. 16. Comparison of CGR316BLi-calculated and experimental [26–27] crack growth rates for unidirectionally 40% CW 316L stainless steel. The CGR316BLi inputs are given in Table 6.

been made electrode potential, temperature and stress dependent, the latter being a new development in terms of the FRDR mechanism but based on literature [17]. Using such a modified FRDR mechanism allowed us to model a consistent set of published crack growth rates [10] and some other independently published crack growth rates [26–27] on cold worked material. It also allowed us to model various trends (Fig. 12) and sensitivities (Fig. 11, Fig. 14). However, the decrease in crack growth rate with the primary water dissolved hydrogen content does not seem to correspond to experimental observations [28]. This leads us to believe that either one has to consider the effect of hydrogen on the crack-tip strain rate, based on hydrogen induced plasticity [29], or that a mechanism other than the FRDR is operative. This does however not render the full model developed here obsolete. Indeed, the full model is based on the calculation of the local crack-tip loading, electrochemical and mechanical and a crack growth rate mechanism. Altering the crack growth rate mechanism does not affect the need to calculate the crack-tip loading. In terms of the modified FRDR mechanism the crack-tip loading is determined by the local electrode potential, the thermal activation energy, the crack-tip stress (34) and the crack-tip strain rate (3). Moving towards a crack growth rate mechanism where grain boundary cohesion is determining crack growth rate one could reason that various activation energies (a thermal activation energy E_a, a mechanical energy $V_m\sigma_{tip}$ and an electrochemical energy αFE_{tip}) affect cohesion and the associated crack growth rate, i.e.

$$\dot{a} \approx \exp\left\{\frac{-E_a + \alpha FE_{tip} + V_m\sigma_{tip}}{RT}\right\}. \quad (36)$$

This equation still requires one to calculate local crack-tip conditions. Here too an additional term could take into account the effect of hydrogen. The cohesion mechanism might explain (1) why a crack-tip opening displacement from LEFM, which is larger than the experimentally observed sharp crack-tip [30], works with the FRDR mechanism and (2) why, apparently, Faraday's law is not being observed in the empirical crack growth rate model used in the PLEDGE code [31]. Indeed, if it are the freshly created side flanks of a sharp crack that are repassivating then (1) the high LEFM crack-tip opening reflects this freshly created surface area which is larger than the experimentally observed sharp crack-tip opening and (2) Faradays law has to be applied to material loss on the freshly created side flanks and not to material loss associated with crack advance.

A further thought might unify the crack-tip current associated with the present implementation of the FRDR mechanism and the cohesion model. Indeed, one could assume that the crack-tip current's role is to embrittle the grain boundary ahead of the crack-tip and then expressions (34) also remains valid and would yield a crack growth rate according to expression (36). Then one could take the added affect of hydrogen into account by changing expression (36) to read

$$\dot{a} \approx \exp\left\{\frac{-E_a + \alpha FE_{tip} + V_m\sigma_{tip} + Q_H}{RT}\right\} \quad (37)$$

where Q_H, an activation energy for hydrogen pick-up and diffusion into the grain boundary ahead of the crack, would take care of an additional grain boundary embrittling agent, i.e. hydrogen.

Figuring out the exact nature of the crack growth mechanism is subject of international research to which we hope to have made some, be it a small, contribution by rigorously calculating with one postulated mechanism (FRDR). Due to the complexity of crack growth rate modelling one can only guarantee that the effect of cold work has been implemented plausibly assuming the FRDR mechanism – the additional implementation in the FRI-Shoji model giving further support. Most, but not all, data for the model have been obtained independently. This too lends some support to the full model. However, not all effects on the parameters have been taken into account, e.g. the effect of electrode potential on m or the effect of temperature on m and i_{MR}. Given that we have used data from various sources and sometimes approximate in the development of the presented model, the agreement between published and calculated results is reasonable and the developed approach could take care of new information about the exact nature of the stress corrosion crack mechanism when and if it becomes available.

9. Conclusions

The developed CGR316BLi code allows one to calculate the crack propagation rate (CPR) of a 316 stainless steel crack in boric acid–lithium hydroxide solutions. The code is based on (1) the film

rupture/dissolution/repassivation (FRDR) mechanism for stress corrosion cracking, (2) the finite element calculation of the environment and (3) an analytical expression for the crack-tip strain rate. The FRDR model – a commonly used model for predicting CPR under stress corrosion cracking conditions – has been extended to cold worked materials by making the bare metal dissolution current density function of stress, i.e.

$$i_0 \approx \exp\left\{\frac{-E_a + \alpha \mathrm{FE} + V_m 2.5\sigma_y}{\mathrm{RT}}\right\}.$$

The code, using the extended model, has been calibrated against literature-published CPR data. Trend calculations have been performed to study the influence of crack length, dissolved hydrogen content, boric acid and lithium hydroxide concentrations, stress intensity, operational cycle, yield strength and work-hardening exponent on CPR. Crack growth rate tests not used in the two-parameter calibration were modelled and the calculated crack propagation rates are in good agreement with the reported ones.

Although good correspondence has been obtained between the extended model and literature published data, the extended model does not proof or disprove the validity of the FRDR mechanism for crack growth. The extended model is however a plausible one and applicable to engineering calculations.

Acknowledgements

The work has been sponsored by SCK•CEN, Tractebel under contract number KNT 90991165 and the European Union's integrated 6th framework project PERFECT under contract number FI6O-CT-2003-508840. The end product, CGR316BLi, was a collaboration between SCK•CEN (Belgian Nuclear Energy Research Centre) and VUB (Vrije Universiteit Brussel).

References

[1] P.M. Scott, Corrosion 56 (8) (2000) 771.
[2] F.P. Ford, P.L. Andresen, Corrosion in nuclear systems: environmentally assisted cracking in light water reactors, in: P. Marcus (Ed.), Corrosion Mechanisms in Theory and Practice, CRC Press, 2002.
[3] F.P. Ford, Slip dissolution model, in: D. Desjardins, R. Oltra (Eds.), Corrosion Sous Contrainte – Phénoménologie et Méchanismes, Bombannes, 1990.
[4] S. Gavrilov, M. Vankeerberghen, G. Nelissen, J. Deconinck, Corros. Sci. 49 (2007) 980.
[5] T. Shoji, K.S. Raja, G.F. Li, Y.J. Lee, A. Brozova, Critical parameters of environmentally assisted cracking in nuclear systems, Corrosion/2000, NACE, Paper 00190, 2000.
[6] M.M. Hall Jr., Corros. Sci. 50 (2008) 2902.
[7] A. Turnbull, Corros. Sci. 39 (1997) 789.
[8] J.S. Newman, Electrochemical Systems, second Ed., Prentice-Hall, 1991.
[9] G. Nelissen, A. Van Theemsche, C. Dan, B. Van den Bossche, J. Deconinck, J. Electroanal. Chem. 563 (2) (2004) 213.
[10] K. Arioka, T. Yamada, T. Terachi, G. Chiba, Corrosion 63 (12) (2007) 1114.
[11] M. Vankeerberghen, A mechano-electrochemical diagram for crack growth under EAC conditions, Corrosion/2004, Paper No. 04573, NACE, 2004.
[12] Materials Reliability Program (Disposition curves), EPRI, Palo Alto, CA: e.g. MRP-115 2004 1006696.
[13] M. Jürgensen, H. Neder, D. Wolter, U. Staudt, S. Odar, V. Schneider, VGB guideline for the water in nuclear power plants with light water reactors (PWR) VGB-R 401 J, 2006.
[14] A. Turnbull, Corros. Sci. 39 (4) (1997) 789.
[15] D.D. Macdonald, M. Urquidi-Macdonald, Corros. Sci. 32 (1) (1991) 51.
[16] M. Vankeerberghen, D.D. Macdonald, Corros. Sci. 44 (2002) 1425.
[17] E.M. Gutman, Mechanochemistry of Solid Surfaces, World Scientific Publishing, 1994, ISBN: 9810217811.
[18] T.L. Anderson, Fracture Mechanics – Fundamentals and Applications, Taylor and Francis, 2005, pp. 75 and 114, ISBN: 0-8493-1656-1.
[19] R.M. McMeeking, D.M. Parks, On criteria for J-dominance of crack tip fields in large-scale yielding, in: Elastic Plastic Fracture, ASTM STP 668, 1979, p. 175.
[20] T. Shoji, S. Suzuki, R.G. Ballinger, Theoretical prediction of SCC growth behavior, in: Proceedings of the Seventh International Symposium Environmental Degradation of Materials in Nuclear Power Systems – Water Reactors, vol. 1, 1995, pp. 881–889.
[21] T. Shoji, Z. Lu, Q. Peng, S. Wang, Y. Takeda, A. Kai, Pres. Ves. Pip. 479 (2004) 175.
[22] P.L. Andresen, F.P. Ford, Mater. Sci. Eng. A 103 (1988) 167.
[23] P.L. Andresen, F.P. Ford, Int. J. Pres. Ves. Pip. 59 (1994) 61.
[24] P.L. Andresen, M.M. Morra, Corrosion 64 (1) (2008) 15.
[25] P.L. Andresen, SCC mitigation strategies in hot water, Corrosion/1997, Paper No. 102, NACE, 1997.
[26] L. Duisabeau, L. Fournier, A. Toivonen, P. Aaltonen, SCC growth rate quantification in CW 316L stainless steel in PWR primary water using reduced size compact tension specimens, in: Proceedings of the Fontevraux 6, Sixth International Symposium Contributions of Materials Investigations to Improve the Safety and Performance of LWRs, 2006.
[27] C. Guerre, O. Raquet, E. Herms, M. Le Calvar, G. Turluer, SCC growth behavior of austenitic stainless steels in PWR primary water conditions, in: Proceedings of the 12th International Symposium Environmental Degradation of Materials in Nuclear Power Systems – Water Reactors, 2005, pp. 1029–1036.
[28 Various private communications.
[29] D. Delafosse, T. Magnin, Eng. Fract. Mech. 68 (2001) 693.
[30] R.W. Staehle, Critical analysis of 'tight cracks', in: Proceedings of the 13th International Symposium Environmental Degradation of Materials in Nuclear Power Systems – Water Reactors, 2007.
[31] D.D. Macdonald, Corros. Sci. 38 (6) (1996) 1003.